POLITECNICO DI TORINO
Repository ISTITUZIONALE

High-performance ceria via supramolecular metal–organic gel precursors for visible-light-driven hydrogen evolution from aqueous glucose

Original
High-performance ceria via supramolecular metal–organic gel precursors for visible-light-driven hydrogen evolution from aqueous glucose / Muscatello, A., Iervolino, G., Vaiano, V., Esposito, S.. - In: CHEMICAL COMMUNICATIONS. - ISSN 1359-7345. - 61:81(2025), pp. 15830-15833. [10.1039/d5cc04076k]

Availability:
This version is available at: 11583/3006198 since: 2025-12-28T13:21:56Z

Publisher:
The Royal Society of Chemistry - RSC

Published
DOI:10.1039/d5cc04076k

Terms of use:

This article is made available under terms and conditions as specified in the corresponding bibliographic description in the repository

Publisher copyright

(Article begins on next page)

26 November 2026

ChemComm

COMMUNICATION

View Article Online
View Journal | View Issue

Check for updates

Cite this: *Chem. Commun.*, 2025, **61**, 15830

Received 19th July 2025,
Accepted 4th September 2025

DOI: 10.1039/d5cc04076k

rsc.li/chemcomm

Open Access Article. Published on 05 September 2025. Downloaded on 12/28/2025 11:58:19 AM.
This article is licensed under a Creative Commons Attribution 3.0 Unported Licence.

High-performance ceria *via* supramolecular metal–organic gel precursors for visible-light-driven hydrogen evolution from aqueous glucose

Andrea Muscatello,[a] Giuseppina Iervolino,*[b] Vincenzo Vaiano[b] and Serena Esposito *[a]

A supramolecular cerium-based metal–organic gel (MOG) was used as a soft precursor to prepare a defect-rich CeO_2 photocatalyst. The resulting material exhibited enhanced visible-light-driven hydrogen evolution from glucose, outperforming conventionally synthesized ceria. Spectroscopic analysis revealed higher oxygen vacancy content and improved charge separation, highlighting the potential of MOG-derived photocatalysts.

Hydrogen is a promising alternative to fossil fuels due to its high energy density and carbon-free combustion. Among various production methods, photocatalysis has attracted considerable attention for its ability to harness solar energy, an abundant and renewable resource. Certain food-processing wastewaters are particularly rich in glucose and other sugars, providing a biomass-derived feedstock for sustainable hydrogen generation. In this context, photocatalytic hydrogen production *via* glucose decomposition in aqueous solution has emerged as a low-cost and practical strategy to support the transition to hydrogen-based energy systems.[1–4] The development of efficient photocatalytic systems for this purpose relies heavily on the design of advanced functional materials. In this scenario, metal–organic gels (MOGs) have recently gained interest as versatile precursors for oxide-based photocatalysts, owing to their tuneable structural and textural properties. Indeed, MOGs represent an intriguing class of soft materials, structurally related to metal–organic frameworks (MOFs) but generally less ordered. MOGs form *via* rapid aggregation of metal–ligand clusters under supramolecular interactions, though some degree of coordinative cross-linking may occur.[5–9] The synthesis of MOGs is characterized by mild reaction conditions, simplicity of equipment, and low production costs. This ease of fabrication, combined with the flexibility in self-assembly of the diverse building blocks, provides significant versatility in achieving targeted structural control and functional diversification. These attributes position MOGs as highly attractive materials for advanced applications.[10,11] In this scenario, careful tuning of the synthesis parameters becomes crucial, as it enables precise control over supramolecular self-assembly across multiple length scales, leading directly to the preparation of targeted gel architectures. Key parameters include the choice of metal source, water content, and reactant concentrations.[12,13]

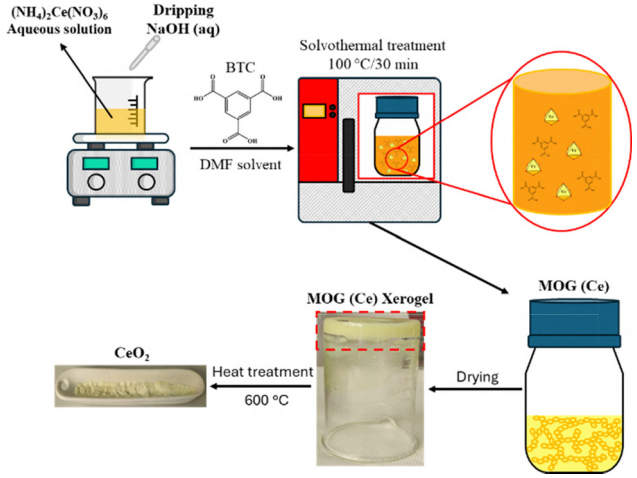
One of the most compelling aspects of MOGs lies in their potential as sacrificial templates for the synthesis of advanced functional materials, particularly metal oxides.[14] Through controlled thermal treatments, such as combustion or pyrolysis, the organic components of the MOG can be removed, leaving behind the metal oxide while largely preserving the nanoscale architecture and homogeneity inherited from the parent gel.[15] The "gel-to-oxide" transformation offers significant advantages over traditional synthesis methods, allowing for precise control over structural, surface and textural properties, which are critical parameters for optimizing material performance.[10,16–18] Specifically, we aim to exploit the intrinsic properties of MOGs to prepare highly efficient CeO_2 photocatalysts for hydrogen evolution from aqueous solutions containing organic sacrificial agents (*e.g.*, glucose), as CeO_2 is known to promote photocatalytic hydrogen production from a variety of organic compounds in aqueous media.[19,20]

Herein, we propose the synthesis of cerium dioxide nanoparticles *via* the controlled combustion of a cerium-based metal–organic gel. The MOG precursor was prepared using a one-pot solvothermal approach where $(NH_4)_2Ce(NO_3)_6$ and benzene-1,3,5-tricarboxylic acid (BTC) were selected as building blocks. A systematic variation of the synthesis parameters, such as cerium precursor concentration, the Ce : BTC molar ratio, the molar amount of NaOH, and the quantity of DMF solvent, was adopted to control gel formation, specifically distinguishing between flowing and non-flowing gel states. This

[a] *Department of Applied Science and Technology, Politecnico di Torino, Corso Duca degli Abruzzi 24, 10129 Torino, Italy. E-mail: serena_esposito@polito.it*
[b] *Department of Industrial Engineering, University of Salerno, Via Giovanni Paolo II 132, 84084 Fisciano, SA, Italy. E-mail: giiervolino@unisa.it*

This journal is © The Royal Society of Chemistry 2025

Open Access Article. Published on 05 September 2025. Downloaded on 12/28/2025 11:58:19 AM.
This article is licensed under a Creative Commons Attribution 3.0 Unported Licence.



Scheme 1 Scheme of the preparation route of MOG (Ce) and derived CeO_2-MOG by heat treatment in air.

meticulous investigation allowed us to precisely understand the impact of each variable on the gelation process, enabling the optimization of the synthesis procedure (see SI "Summary of the systematic variation of synthesis parameters"). The MOG gel precursor was characterized by thermogravimetric analysis (TGA) and X-ray diffraction (XRD) to confirm its thermal and structural properties (Fig. S1 and S2, SI). This optimized approach directly led to the successful formation of the Ce-MOG xerogel after solvent removal, as depicted in Scheme 1. Subsequently, the Ce-MOG xerogel was calcined in air at temperatures up to 600 °C to yield cerium oxide. This temperature was selected based on TGA analysis of the gel (Fig. S1, SI). To highlight the advantages of our approach, the resulting CeO_2-MOG was directly compared with CeO_2-P, a reference ceria sample prepared *via* the conventional precipitation method.

Highly crystalline cerium oxide with its characteristic fluorite structure was successfully obtained by combustion of Ce-MOG, as confirmed by comparison with CeO_2-P (Fig. S3, SI).

Crucially, this synthesis pathway *via* the MOG precursor resulted in a material with markedly different textural properties compared to the conventionally prepared CeO_2-P, highlighting the profound influence of the synthesis route on the final catalyst characteristics.

While both catalysts exhibit type II N_2 adsorption–desorption isotherms at 77 K (Fig. S4, SI), their contrasting hysteresis loops reveal distinct porous textures. The MOG-derived ceria displays an H3-type hysteresis, consistent with a more open mesoporous network, while the precipitated sample shows an H4-type loop, typically associated with narrow slit-like pores and the presence of microporosity. Textural data are summarized in Table 1. The CeO_2-P showed a relatively high specific surface area (SSA) of 81 $m^2\ g^{-1}$ but a low total pore volume of 0.05 $cm^3\ g^{-1}$, suggesting the predominance of small pores likely in the microporous to narrow mesoporous range. In contrast, the CeO_2-MOG exhibited a significantly lower SSA of 22 $m^2\ g^{-1}$ but a higher total pore volume of 0.1 $cm^3\ g^{-1}$,

Table 1 Summary of the textural data of catalysts prepared by MOG combustion and conventional precipitation

	SSA ($m^2\ g^{-1}$)	Micropore volume ($cm^3\ g^{-1}$)	External surface area ($m^2\ g^{-1}$)	Total pore volume ($cm^3\ g^{-1}$)
CeO_2-MOG	22	0.0008	19.8	0.10
CeO_2-P	81	0.0033	73.3	0.05

indicative of a mesoporous or even partially macroporous structure.

Fig. 1a shows the Raman spectra of the CeO_2-MOG and CeO_2-P samples. Both spectra exhibit a prominent peak at ~465 cm^{-1}, which corresponds to the F_2g symmetric stretching mode of the fluorite cubic phase of CeO_2,[21,22] confirming the formation of crystalline ceria in both materials. Notably, CeO_2-MOG displays a broader signal, indicating a greater degree of structural disorder. In addition, the CeO_2-MOG spectrum reveals distinct defect-related D-modes in the 550–650 cm^{-1} region, which are significantly less pronounced in the CeO_2-P sample. These features are typically associated with oxygen vacancies and lattice defects,[23] suggesting that the MOG-derived synthesis route promotes the formation of a more defective ceria network. The defect content was qualitatively assessed by the intensity ratio between the D-mode (~600 cm^{-1}) and the F_2g mode (~465 cm^{-1}). The I_D/I_{F2g} ratio

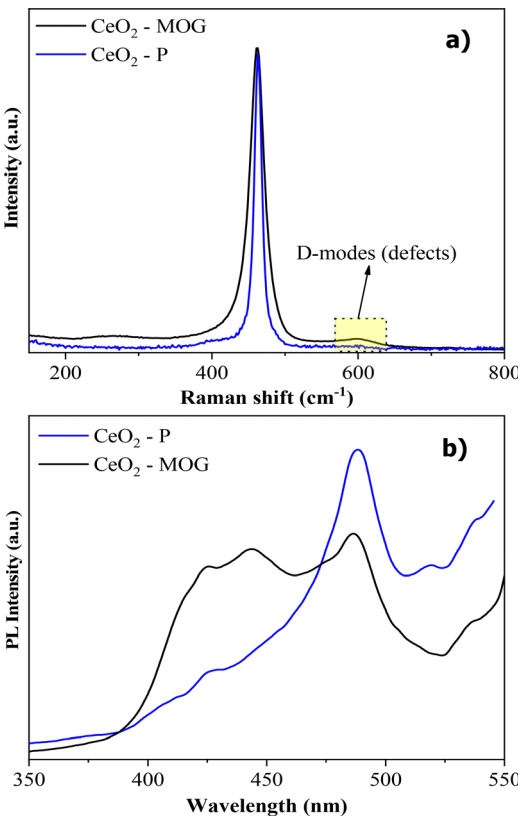


Fig. 1 (a) Raman spectra of CeO_2-P and CeO_2-MOG photocatalysts. (b) Photoluminescence spectra of CeO_2-P and CeO_2-MOG samples.

Open Access Article. Published on 05 September 2025. Downloaded on 12/28/2025 11:58:19 AM.
This article is licensed under a Creative Commons Attribution 3.0 Unported Licence.

increases from ~0.002 for CeO_2-P to ~0.004 for CeO_2-MOG, indicating a higher density of structural defects in the latter; this ratio is routinely used to assess the oxygen vacancy level in ceria-based materials.[24] Critical insights into the defect and electronic structure were provided by photoluminescence spectroscopy (PL) (Fig. 1b). This technique, which reveals information on electron–hole pair dynamics, confirms the existence of defect energy levels within the band gap, attributed to both Ce^{3+} sub-bands and oxygen vacancies. Nevertheless, the emission spectra of CeO_2-P and CeO_2-MOG revealed distinct peak profiles. The most intense peak at 488 nm (green-blue region), attributable to $F^{+*} \rightarrow F^{+}$ emission, where F^{+} is defect state related to oxygen vacancies containing 1 electron and F^{+*} is an excited state close to the conduction band, is notably less intense for CeO_2-MOG.[25] This reduced intensity indicates an increased carrier lifetime in CeO_2-MOG, suggesting different recombination dynamics and, potentially, a greater availability of electrons for surface redox processes.

Another noteworthy feature of the CeO_2-MOG sample is the richer presence of bands in the 380–460 nm range, which are hardly visible in CeO_2-P. Specifically, the bands at 425 nm and 443 nm are associated with the Ce^{3+} $4f^1$ state located 1.3–1.5 eV above the valence band.[26] This suggests that CeO_2-MOG possesses a more defective nature compared to the CeO_2-P sample. The time-resolved H_2 production profiles for CeO_2-P and CeO_2-MOG are reported in Fig. 2; for direct comparison, the values at 240 minutes of visible-light irradiation were considered. CeO_2-MOG exhibits a significantly higher H_2 evolution rate than the reference CeO_2-P, reaching over 11 000 μmol L^{-1} after 240 minutes.

This clearly highlights the superior photocatalytic performance of CeO_2-MOG, underscoring how synthesis conditions are paramount in tailoring the functional features of CeO_2-based catalysts. Given their nearly identical band gap energies (~2.96 eV as shown by Tauc plot (Fig. S5, SI)), differences in visible-light absorption cannot account for the improved photocatalytic activity of CeO_2-MOG. Instead, the improved performance is closely related to the structural and electronic properties of the material. Raman spectroscopy (Fig. 1a) reveals a more intense signal in the 550–650 cm^{-1} region for CeO_2-MOG, indicative of a higher concentration of oxygen vacancies.

This is corroborated by PL measurements (Fig. 1b), where CeO_2-MOG shows markedly lower emission intensity compared to CeO_2-P, suggesting reduced radiative recombination of photogenerated carriers. Moreover, the broader and slightly red-shifted PL band observed for CeO_2-MOG implies the presence of defect-related sub-bandgap states, such as Ce^{3+} sites and oxygen vacancy levels, which can trap charge carriers and prolong their lifetime, thereby enhancing the probability of interfacial redox reactions. These observations are in line with previous findings on oxygen vacancy-rich CeO_2-based photocatalysts, which demonstrated enhanced H_2 evolution efficiency due to defect-mediated charge transport pathways.[27] In addition to its superior H_2 evolution, CeO_2-MOG also exhibited a higher CO_2 production compared to CeO_2-P under the same reaction conditions. The time-resolved CO_2 production profiles are reported in Fig. S6 (SI). This observation suggests a more efficient and complete oxidative decomposition of the organic sacrificial agent (*e.g.*, glucose), which is consistent with the enhanced photocatalytic activity of the MOG-derived material. The increased CO_2 yield supports the hypothesis that CeO_2-MOG promotes more effective charge carrier separation and utilization, facilitating both reduction (H_2 evolution) and oxidation (organic degradation) half-reactions.

The reusability of the CeO_2-MOG photocatalyst was assessed over six consecutive photocatalytic cycles under visible-light irradiation (Fig. 3). After each 4-hour cycle, the catalyst was recovered by centrifugation, thoroughly washed with deionized water, and dried before reuse. As shown in Fig. 3, CeO_2-MOG retained nearly constant hydrogen production throughout all six cycles, with a negligible decrease in activity (<2%), well

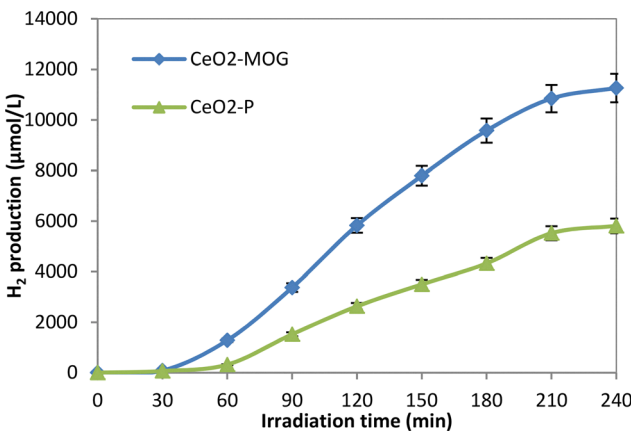


Fig. 2 Hydrogen production over CeO_2-P (prepared with conventional precipitation synthesis), and CeO_2-MOG_2 photocatalysts during 4 hours of visible light irradiation. Reaction conditions: catalyst dosage = 2 g L^{-1}; initial glucose concentration = 250 mg L^{-1}; solution volume = 80 mL; light source = four visible light lamps (8 W each, 400–700 nm).

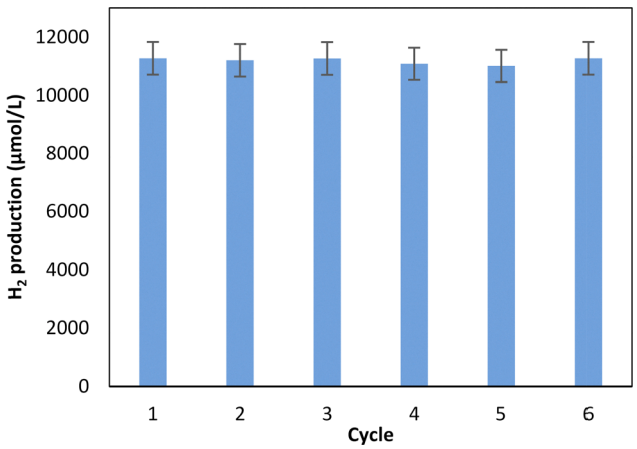


Fig. 3 Reusability test of CeO_2-MOG for photocatalytic hydrogen production under visible-light irradiation over six consecutive cycles. Reaction conditions: glucose concentration = 250 mg L^{-1}; catalyst dosage = 2 g L^{-1}; solution volume = 80 mL; irradiation time = 4 hours per cycle; light source = four visible-light lamps (8 W each, 400–700 nm).

This journal is © The Royal Society of Chemistry 2025

Open Access Article. Published on 05 September 2025. Downloaded on 12/28/2025 11:58:19 AM.
This article is licensed under a Creative Commons Attribution 3.0 Unported Licence.

within the experimental margin of error. This excellent cycling stability underscores the structural and chemical robustness of the CeO_2-MOG material under the adopted operational conditions.

In summary, a supramolecular metal–organic gel was successfully employed as a soft template for the synthesis of defect-rich CeO_2 nanoparticles, enabling enhanced photocatalytic hydrogen production from glucose under visible-light irradiation. Compared to conventionally prepared ceria, the MOG-derived catalyst exhibited a higher concentration of oxygen vacancies, improved charge carrier separation, and superior overall activity. The excellent recyclability over multiple cycles further highlights the robustness of the material under operating conditions. These findings demonstrate the potential of MOG-based routes for the rational design of advanced metal oxide photocatalysts for sustainable hydrogen generation from biomass-derived organics.

Conflicts of interest

There are no conflicts to declare.

Data availability

The data supporting this article have been included as part of the SI. Supplementary information: Experimental, and details of the results. See DOI: **10.1039/d5cc04076k**.

Notes and references

1 A. Mancuso and G. Iervolino, *Catalysts*, 2022, **12**, 1074.
2 Y. Li, J. Wang, S. Peng, G. Lu and S. Li, *Int. J. Hydrogen Energy*, 2010, **35**, 7116–7126.
3 X. Fu, J. Long, X. Wang, D. Y. Leung, Z. Ding, L. Wu, Z. Zhang, Z. Li and X. Fu, *Int. J. Hydrogen Energy*, 2008, **33**, 6484–6491.
4 K. A. Davis, S. Yoo, E. W. Shuler, B. D. Sherman, S. Lee and G. Leem, *Nano convergence*, 2021, **8**, 6.
5 J. Zhang and C.-Y. Su, *Coord. Chem. Rev.*, 2013, **257**, 1373–1408.
6 B. Zhang, J. Zhang, Y. Zhang, Q. Zuo and H. Zheng, *Langmuir*, 2023, **39**, 10892–10903.
7 L. Casimiro, F. Volatron, G. Boivin, B. Abécassis, S. Alves, D. Brouri, D. Montero, J.-M. Guigner, L.-M. Chamoreau and G. Gontard, *JACS Au*, 2024, **4**, 4948–4956.
8 B. Bueken, N. Van Velthoven, T. Willhammar, T. Stassin, I. Stassen, D. A. Keen, G. V. Baron, J. F. Denayer, R. Ameloot and S. Bals, *Chem. Sci.*, 2017, **8**, 3939–3948.
9 J. Hou, A. F. Sapnik and T. D. Bennett, *Chem. Sci.*, 2020, **11**, 310–323.
10 S. Ma, J. Xu, S. Sohrabi and J. Zhang, *J. Mater. Chem. A*, 2023, **11**, 11572–11606.
11 Z. Zhuang, Z. Mai, T. Wang and D. Liu, *Coord. Chem. Rev.*, 2020, **421**, 213461.
12 F. Zhao, W. Yang, Y. Han, X. Luo, W. Tang, T. Yue and Z. Li, *Chem. Eng. J.*, 2021, **407**, 126744.
13 Z. Lin, J. J. Richardson, J. Zhou and F. Caruso, *Nat. Rev. Chem.*, 2023, **7**, 273–286.
14 J.-C. Huang, Y.-H. Shih, S. Lirio, S.-Y. Wu, H.-T. Chen, W.-L. Liu, C.-H. Lin and H.-Y. Huang, *Chem. Commun.*, 2019, **55**, 4475–4478.
15 Z. Cao, Z. Jiang, Y. Li, C. Huang and Y. Li, *ChemSusChem*, 2019, **12**, 2480–2486.
16 H. Wang, B. H. Chen and D. J. Liu, *Adv. Mater.*, 2021, **33**, 2008023.
17 N. Clayden, A. Aronne, S. Esposito and P. Pernice, *J. Non-Cryst. Solids*, 2004, **345**, 601–604.
18 S. Esposito, *Sol-Gel Synthesis Strategies for Tailored Catalytic Materials*, Springer, 2023, pp. 33–41.
19 G. Iervolino, V. Vaiano, D. Sannino, F. Puga, J. A. Navío and M. C. Hidalgo, *Catalysts*, 2021, **11**, 1558.
20 A. A. Yadav, Y. M. Hunge and S.-W. Kang, *Catalysts*, 2022, **12**, 1185.
21 W. Weber, K. Hass and J. McBride, *Phys. Rev. B: Condens Matter Mater. Phys.*, 1993, **48**, 178.
22 E. Sediva, A. J. Carrillo, C. Halloran and J. L. Rupp, *ACS Appl. Energy Mater.*, 2021, **4**, 1474–1483.
23 V. Araújo, W. Avansi, A. H. de Carvalho, M. Moreira, E. Longo, C. Ribeiro and M. I. B. Bernardi, *CrystEngComm*, 2012, **14**, 1150–1154.
24 F. Liu, Z. Wang, D. Wang, D. Chen, F. Chen and X. Li, *Catalysts*, 2019, **9**, 288.
25 G. Iervolino, O. Tammaro, M. Fontana, B. Masenelli, A. D. Lamirand, V. Vaiano and S. Esposito, *J. Energy Chem.*, 2025, **101**, 263–277.
26 K. Sudarshan, V. Tiwari, P. Utpalla and S. Gupta, *Inorg. Chem. Front.*, 2019, **6**, 2167–2177.
27 Y.-P. Qiu, W.-Z. Wang, M.-H. Chen, Q. Shi, Z.-Q. Yang and P. Wang, *J. Mater. Chem. A*, 2021, **9**, 18385–18392.